

Article

Hydrogen Evolution Reaction Property of Molybdenum Disulfide/Nickel Phosphide Hybrids in Alkaline Solution

Fan Yang, Ning Kang, Jiayun Yan, Xiuli Wang, Jun He, Siyue Huo and Laizhou Song * 

College of Environmental and Chemical Engineering, Yanshan University, Qinhuangdao 066004, China; m15903396256@163.com (F.Y.); m18332559448@163.com (N.K.); yanjiayun0327@163.com (J.Y.); xlwang790412@163.com (X.W.); hejun@ysu.edu.cn (J.H.); s15930599589@163.com (S.H.)

* Correspondence: songlz@ysu.edu.cn; Tel.: +86-335-838-7741; Fax: +86-335-806-1569

Received: 9 March 2018; Accepted: 14 May 2018; Published: 16 May 2018



Abstract: The hydrogen evolution reaction (HER) property of molybdenum disulfide (MoS_2) is undesirable because of the insufficient active edge sites and the poor conductivity. To enhance HER performance of MoS_2 , nickel phosphide (Ni_2P) was combined with this catalyst and three $\text{MoS}_2/\text{Ni}_2\text{P}$ hybrids (38 wt % Ni_2P addition for $\text{MoS}_2/\text{Ni}_2\text{P}$ -38, 50 wt % Ni_2P addition for $\text{MoS}_2/\text{Ni}_2\text{P}$ -50, and 58 wt % Ni_2P addition for $\text{MoS}_2/\text{Ni}_2\text{P}$ -58) were fabricated via a hydrothermal synthesis process. Morphologies, crystallinities, chemical components, specific surface areas, and HER properties of the fabricated $\text{MoS}_2/\text{Ni}_2\text{P}$ samples in an alkaline electrolyte were characterized and tested. In addition, the insight into the HER properties of as-prepared catalysts were revealed by the density functional theory (DFT) calculation. Additionally, the stabilities of pure MoS_2 , Ni_2P , and $\text{MoS}_2/\text{Ni}_2\text{P}$ -50 samples were evaluated. The results show that the addition of Ni_2P can enhance the HER property of the MoS_2 catalyst. Although HER properties of the above-mentioned three $\text{MoS}_2/\text{Ni}_2\text{P}$ hybrids are inferior to that of pure Ni_2P , they are much higher than that of MoS_2 . Among as-prepared three hybrids, $\text{MoS}_2/\text{Ni}_2\text{P}$ -50 exhibits the best HER performance, which may be due to its uniform morphology, large specific surface area, and excellent stability. The $\text{MoS}_2/\text{Ni}_2\text{P}$ -50 hybrid shows a high cathodic current density (70 mA/cm^2 at -0.48 V), small Tafel slope (~ 58 mV/decade), and a low charge transfer resistance (0.83 $\text{k}\Omega\cdot\text{cm}^2$).

Keywords: hydrogen evolution reaction; molybdenum disulfide; nickel phosphide; hydrothermal synthesis; density functional theory; alkaline electrolyte

1. Introduction

With growing concerns about environmental pollution and energy crises resulting from overconsumption of coal and fossil fuels, the exploitation of renewable clean energies, such as solar energy, wind energy, hydraulic power, biological energy, fuel cell, and hydrogen energy come to the forefront [1–3]. Among the clean energies mentioned above, hydrogen energy is attracting ever-growing attention due to the convenient production and effective cost [4,5]. Apart from the traditional method through steam from fossil fuels, the process of electrochemical water splitting is considered as an alternative to produce hydrogen through the HER [6–9]. Until the present, the well-known platinum and platinum-based alloys show the best electrocatalytic performance for HER [10–13]. However, their high-cost and scarcity impede their wide applications in practice [14–16].

To facilitate HER application, it is urgent to develop low-cost alternatives with Earth-abundant and cost-effective features to replace the noble metals [17,18]. Thus, various non-noble materials including transition metal sulfides [19], selenides [20], oxides [21], carbides [22], and nitrides [23],

as well as phosphides [24], have been reported as electrocatalysts for HER. Among these catalysts, MoS₂-based materials have been researched as the promising substitutes owing to their low cost, Earth-abundance, and the relatively high activity [25,26]. However, the inert basal surface, poor intrinsic conductivity, and insufficient edged activity sites limit their HER performance [27]. In order to enhance the HER performance of this catalyst efficiently, a large number of efforts have been devoted and can be briefly classified as follows [4,28,29]: (1) increasing the density of active edge sites; (2) enhancing the inherent activity; (3) improving the electrical contact between active sites. Generally, intensive endeavors such as interlayer intercalation [30,31], phase transformation (from 2H-MoS₂ to 1T-MoS₂) [32], gentle oxidation [33], functional structural design [34], and stabilizing the edge layers with organic molecules [35] have been made to increase the active sites located at the edge, whereas the basal plane is still chemically inert.

Additionally, for the purpose of improving the electrical contact between active sites of MoS₂, various promoters, such as gold [30], platinum [36], palladium [37], carbon materials [38], core-shell MoO₃ [39], Co₃O₄ nanosheet array [40], graphene [41,42], graphene oxide [17,43], and nickel-phosphorus (Ni-P) powders [4], have been adopted as electrical conduction-enhancing supports. Of all the above-mentioned supports, the cost-effective Ni-P powder possesses superior electrical conductivity and outstanding HER performance [28,44,45]. Thus, this material is a suitable candidate employed to enhance the HER activity of MoS₂. In view of the fact that Ni-P incorporation is advantageous to the enhancement in the HER property of MoS₂ [4], herein, it should be worth noting that the coexistent nickel phosphide phases (i.e., Ni₅P₂, Ni₂P, Ni₃P, Ni₁₂P₅, NiP₂, Ni₅P₄, NiP, and Ni₇P₃) [46] will play a major role in HER feature of this catalyst. Among these nickel phosphides, Ni₂P demonstrates an excellent HER characteristic [14,47] and draws tremendous attention. Although the attempt of incorporation of Ni₂P on to the surface of nano-MoS₂ has been made in the hope of the increment in HER performance [16]; to the best of our knowledge so far, the effort of Ni₂P employed as a sublayer support to improve the HER property of MoS₂ is insufficient. In this sense, the role of Ni₂P as a layer support in pursuit of the increase in MoS₂ HER deserves to be investigated.

Unambiguously, the density functional theory (DFT) calculations as a major supplement to experimental techniques will be significantly valuable for revealing the intrinsic feature of HER [30,42,48–50]. Atomistic details related to the adsorption and desorption of hydrogen atoms, as well as the immanent interaction between hydrogen atom and the catalyst can be perfectly interpreted. To date, some studies in HER process for MoS₂, Ni₂P, and MoS₂/graphene catalysts have been reported [42,49,50], but efforts related to that of MoS₂/graphene hybrid catalyst via the DFT simulation are insufficient.

In this work, MoS₂ was anchored on the surface of the Ni₂P nanosheet via a hydrothermal synthesis process, and the three MoS₂/Ni₂P hybrids (38 wt % Ni₂P addition for MoS₂/Ni₂P-38, 50 wt % Ni₂P addition for MoS₂/Ni₂P-50, and 58 wt % Ni₂P addition for MoS₂/Ni₂P-58) were fabricated. The aim of this study is to offer an effective route to improve the HER property of MoS₂ by combining of this metal sulfide with Ni₂P. Morphologies, crystallinities, chemical components, and active areas of the prepared MoS₂/Ni₂P hybrids were characterized by X-ray diffraction (XRD), scanning electron microscopy (SEM), transmission electron microscopy (TEM), X-ray photoelectron spectroscopy (XPS), and the Brunauer-Emmett-Teller (BET) method. Techniques of linear sweep voltammetry (LSV), Tafel polarization, cyclic voltammetry (CV), and electrochemical impedance spectroscopy (EIS) were employed to test HER properties of the above three hybrids; subsequently, the effect of Ni₂P as the bottom substrate was illustrated. Additionally, the adsorption energies (ΔE_{ads}) and the Gibbs free energies of adsorption (ΔG_{ads}) between the hydrogen atoms and the catalyst were calculated. Furthermore, the stability of the hybrid was evaluated.

2. Experimental Section

2.1. Material

Analytical grade reagents of ammonium molybdate tetrahydrate ($(\text{NH}_4)_6\text{Mo}_7\text{O}_{24}\cdot 4\text{H}_2\text{O}$, 99 wt %), thiourea ($\text{CH}_4\text{N}_2\text{S}$, 99 wt %), red phosphorus, nickel chloride hexahydrate ($\text{NiCl}_2\cdot 6\text{H}_2\text{O}$, 98 wt %), potassium hydroxide (KOH), and absolute ethanol were purchased from Jingchun Scientific Co. Ltd. (Shanghai, China). The 5 wt % of Nafion solution was offered by Alfa Aesar Chemicals Co. Ltd. (Shanghai, China). The Pt/C power (20 wt % Pt on Vulcan XC-72R) was supplied by Yu Bo Biotech Co. Ltd. (Shanghai, China). In this present study, all above reagents were used as received in the present study and without further purification.

2.2. Synthesis of the Ni_2P Nanosheet

Under vigorous stirring condition, 1.63 g red phosphorus and 1.25 g $\text{NiCl}_2\cdot 6\text{H}_2\text{O}$ were dissolved in 15 mL deionized water for 30 min and a slurry-like mixture was obtained. Then this mixture solution was transferred into a 25 mL Teflon-lined stainless steel autoclave and followed by placed into a muffle furnace (WRN-010, Eurasian, Tianjin, China), which was preheated to 180 °C. The hydrothermal synthesis process was carried out at 180 °C for 24 h. When the temperature of the muffle furnace was cooled to room temperature naturally, the formed particles were separated by centrifugation and washed with ethanol twice and deionized water three times. Lastly, the fabricated gray-black Ni_2P powders were dried in a vacuum oven (DZF-6050, Boxun Industrial Co. Ltd., Shanghai, China) and retained for use.

2.3. Synthesis of the $\text{MoS}_2/\text{Ni}_2\text{P}$ Hybrids

A total of 1.41 g $(\text{NH}_4)_6\text{Mo}_7\text{O}_{24}\cdot 4\text{H}_2\text{O}$, 0.26 g $\text{CH}_4\text{N}_2\text{S}$ and three different amounts of Ni_2P (38 wt %, 50 wt %, and 58 wt %) were dispersed in 20 mL of distilled water. The mixture solution was vigorously stirred for 1 h at room temperature. After that, the solution was transferred into a 25 mL Teflon-lined stainless steel autoclave placed in a muffle furnace, and then reacted at 200 °C for 24 h. As the solution temperature was cooled to room temperature naturally, the resultant three black samples ($\text{MoS}_2/\text{Ni}_2\text{P}$ -38, $\text{MoS}_2/\text{Ni}_2\text{P}$ -50, and $\text{MoS}_2/\text{Ni}_2\text{P}$ -58) were centrifuged and adequately washed with ethanol and deionized water. Finally, the as-synthesized samples were dried under a vacuum atmosphere at 60 °C for 12 h.

2.4. Characterization

Crystal structures of the synthesized $\text{MoS}_2/\text{Ni}_2\text{P}$ samples were determined by an X-ray diffractometer (XRD, SmartLab, Tokyo, Japan) using Cu $K\alpha$ radiation ($\lambda = 1.5418 \text{ \AA}$) from 5 to 100 angles at a scanning rate of 5°/min. The morphologies of the samples were obtained using a scanning electron microscope (SEM, S-4800, Hitachi, Tokyo, Japan) at an accelerating voltage of 5 kV. The elemental compositions and chemical states of these three $\text{MoS}_2/\text{Ni}_2\text{P}$ samples were characterized by X-ray photoelectron spectra (XPS, ESCALAB MK II, Thermo Fisher Scientific, Waltham, MA, USA) using Mg $K\alpha$ as the excitation source. The Brunauer-Emmett-Teller (BET) specific surface areas of the obtained samples were examined by N_2 adsorption/desorption measurement on a Nova 4000e analyzer (Quantachrome Instrument, Boynton Beach, FL, USA) at 77 K.

2.5. Electrochemical Measurements

Before preparing the working electrode, a glassy carbon electrode (GCE) of 3 mm in diameter was firstly polished with 1000# water sandpaper and cleaned with ethanol and deionized water. Typically, 5 mg of catalyst (Ni_2P , MoS_2 , $\text{MoS}_2/\text{Ni}_2\text{P}$ hybrids, and the commercial 20 wt % Pt/C) and 30 μL Nafion solution (5 wt %) were dispersed in 1 mL solution consisting of 250 μL absolute ethanol and 750 μL deionized water, and followed by sonication for 1 h to form a homogeneous ink. Then, 5 μL of the

dispersion solution was loaded onto the surface of the polished GCE and the electrode was dried at room temperature; herein, the excessive ethanol present in the slurry was removed as much as possible by extending the drying time. Prior to each electrochemical test, the electrolyte solution was degassed by bubbling pure nitrogen gas for 30 min to remove the dissolved oxygen.

All electrochemical tests were conducted in a typical three-electrode system attached to an electrochemical workstation (CHI 650C, Chenhua Co. Ltd., Shanghai, China) in 1.0 mol/L KOH electrolyte. The GCE modified by the MoS₂/Ni₂P hybrids (MoS₂, Ni₂P or Pt/C) acted as the working electrode, while a Ag/AgCl electrode and a platinum foil were employed as the reference and counter electrodes, respectively. The acquired potential values relevant to the Ag/AgCl electrode were converted to the reversible hydrogen electrode (RHE) scale: $E_{\text{RHE}} = E_{\text{Ag/AgCl}} + 0.059 \text{ pH} + 0.209 \text{ V}$, i.e., the value of potential throughout this manuscript is relative to RHE. Linear sweep voltammetry (LSV) was analyzed in the potential of -0.8 to 0.2 V at a scan rate of 2 mV/s . Tafel polarization curves were measured in a potential window of 0.3 – 0.65 V with a scan rate of 2 mV/s . Cyclic voltammetry (CV) tests were conducted in a potential window from -0.6 to 0.8 V at a scan rate of 10 mV/s . The electrochemical impedance spectroscopy (EIS) measurements were carried out at a cathodic overpotential of 0.7 V by employing the sinusoidal signal amplitude of 5 mV ; the frequency ranged from 10^5 to 0.01 Hz.

2.6. Computational Details

The calculations based on DFT were implemented in the Materials Studio DMol³ (version 7.0, Accelrys Inc., San Diego, CA, USA) [50,51]. Pulay's direct inversion in the iterative subspace (DIIS) technique, as well as double numerical plus polarization functions (DNP) and the revised Perdew-Burke-Ernzerhof (RPBE) functional were employed. The effective core potential was applied to treat the core electrons of nickel atoms. With respect to the aqueous HER process, a continuum solvation model (COSMO) was used and water with the dielectric constant of 78.54 as the solvent [52]. In addition, for the purpose of taking into account of the weak interactions (hydrogen bond and van der Waals force), the TS (Tkatchenko-Scheffler) method for DFT-D correction was employed [52].

As is well known, the basal plane of MoS₂ has been validated as chemically inert, thus, only the Mo edge-type structure of this catalyst was considered [30]. Three kinds of geometries for MoS₂, Ni₂P, and MoS₂/Ni₂P catalysts were employed: a $(4 \times 5 \times 1)$ supercell with two S-Mo-S trilayer for MoS₂, a $(2 \times 1 \times 1)$ supercell derived from Ni₂P (111) crystal surface with four layers, and a single $(4 \times 5 \times 1)$ -sized trilayer MoS₂ combined by three $(2 \times 1 \times 1)$ -sized Ni₂P layers for MoS₂/Ni₂P. A vacuum with the thickness of 15 \AA in the z-direction was used to separate neighboring slabs and to minimize the interactions between them. During the calculations, only the first layers of MoS₂ and Ni₂P were relaxed in order to save time and computational cost.

3. Results and Discussion

3.1. Characterization of Samples

3.1.1. X-ray Diffraction (XRD) Analysis

The XRD patterns of MoS₂, Ni₂P, and three MoS₂/Ni₂P hybrids (MoS₂/Ni₂P-38, MoS₂/Ni₂P-50, and MoS₂/Ni₂P-58) are displayed in Figure 1. The characteristics peaks at $2\theta = 33.8^\circ$ and 57.1° (curve 1) can be identified, corresponding to (100) and (110) crystal planes of MoS₂, respectively. Herein, it should be noted that the diffraction peak of (002) plane of MoS₂ is undetected. The absence of the (002) diffraction peak of MoS₂ indicates a low stacking height along this direction [5,53]. As demonstrated in curve 2, the diffraction peaks at $2\theta = 40.71^\circ, 44.61^\circ, 47.34^\circ, 54.19^\circ, 54.96^\circ, 66.37^\circ, 72.4^\circ, 74.9^\circ, 80.5^\circ,$ and 88.6° corresponding to (111), (201), (210), (300), (211), (310), (311), (400), (401), and (321) confirm the presence of hexagonal Ni₂P; besides the above-mentioned peaks, the detectable weak peaks ($2\theta = 30.36^\circ, 31.58^\circ$) may be attributed to the coexistence of Ni₅P₄ phase [54], and another weak peak at

$2\theta = 35.4^\circ$ can be assigned to the presence of Ni_{12}P_5 phase [55]. XRD patterns of the $\text{MoS}_2/\text{Ni}_2\text{P}$ hybrids are presented in curves 3–5. The diffraction patterns of $\text{MoS}_2/\text{Ni}_2\text{P}$ hybrids consist of very weak diffraction peak of MoS_2 , which indicates that the MoS_2 is amorphous [5]. In addition, the diffraction peaks related to MoS_2 and Ni_2P are observed, thus suggesting the successful combination between MoS_2 and Ni_2P . It may be indexed to a proof of the fabrication of $\text{MoS}_2/\text{Ni}_2\text{P}$ hybrid. Compared with pure Ni_2P , the diffraction intensity of Ni_2P crystal for three $\text{MoS}_2/\text{Ni}_2\text{P}$ hybrids becomes weak. However, with the increase of Ni_2P addition, intensities of diffraction peaks attributed to Ni_2P become strong and those of MoS_2 show a descending trend, which indicates that Ni_2P plays a major role in the crystallinity of the hybrids.

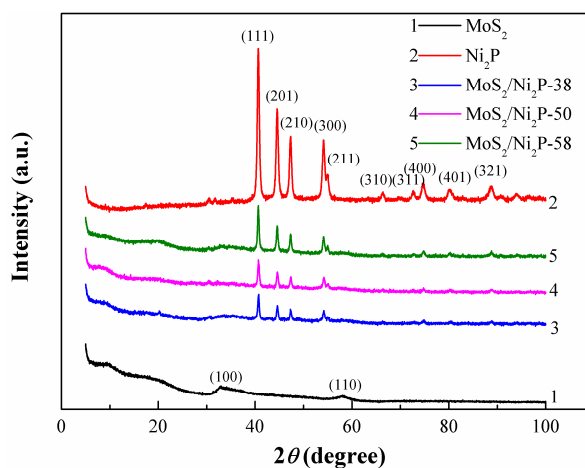


Figure 1. XRD patterns of MoS_2 , Ni_2P , and three $\text{MoS}_2/\text{Ni}_2\text{P}$ hybrids.

3.1.2. Scanning Electron Microscope (SEM)

The morphologies of MoS_2 , Ni_2P , and three $\text{MoS}_2/\text{Ni}_2\text{P}$ hybrids are given in Figure 2. As shown in Figure 2a, the nanoflower-like structure of MoS_2 can be ascertained; of course, there are some nanosheets randomly stacking, which may lead to the decrease in active sites. The fabricated Ni_2P particle exhibits a nanosheet-type morphology (Figure 2b), which would be advantageous to electrochemical conduction among the active sites. Morphologies of the three hybrids are observed in Figure 2c ($\text{MoS}_2/\text{Ni}_2\text{P}$ -38), 2d ($\text{MoS}_2/\text{Ni}_2\text{P}$ -50) and 2e ($\text{MoS}_2/\text{Ni}_2\text{P}$ -58). All of them exhibit a mixed morphology of flower-like and lamellar structures.

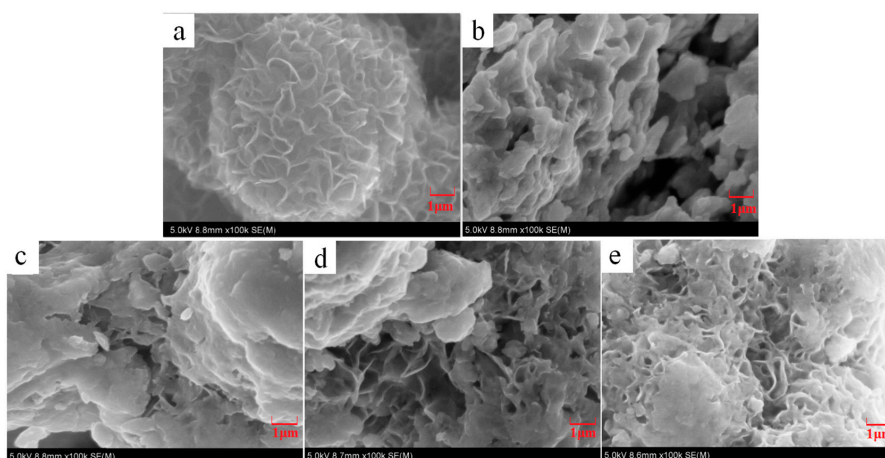


Figure 2. SEM images of MoS_2 , Ni_2P , and three $\text{MoS}_2/\text{Ni}_2\text{P}$ hybrids: (a) MoS_2 ; (b) Ni_2P ; (c) $\text{MoS}_2/\text{Ni}_2\text{P}$ -38; (d) $\text{MoS}_2/\text{Ni}_2\text{P}$ -50; and (e) $\text{MoS}_2/\text{Ni}_2\text{P}$ -58.

As for the SEM pictures of hybrids, with the increasing addition of Ni₂P, the flower-shaped structure can be more easily observed, the presence of the Ni₂P nanosheet will be helpful for the fabrication of MoS₂ nanoflowers. For the sample of MoS₂/Ni₂P-38, the small amount of Ni₂P cannot provide an abundant depositing area, thereby resulting in the serious agglomeration of MoS₂ (Figure 2c). For MoS₂/Ni₂P-50 sample (the mass ratio of MoS₂ and Ni₂P is 1:1), it can be observed that the petal structure and the plate-type structure uniformly coexist (Figure 2d), and more well-proportioned nanoflower-like MoS₂ particles distribute on the surface of Ni₂P. Whereas, for MoS₂/Ni₂P-58 (Figure 2e), with the large addition of Ni₂P, it is explicit that the dense MoS₂ flower structure can be obtained, showing a resemblance to that of MoS₂ (Figure 2a). By a comparison of morphologies of the three hybrids, for the MoS₂/Ni₂P-50 sample, the MoS₂ nanoparticles evenly disperses on the surface of the Ni₂P nanosheet.

3.1.3. X-ray Photoelectron Spectroscopy (XPS)

The elemental compositions and their valences of three MoS₂/Ni₂P hybrids were measured by XPS. The Mo 3d, S 2p, Ni 2p, P 2p and O 1s high-resolution spectra of three MoS₂/Ni₂P hybrids are respectively presented in Figure 3, and the corresponding bond energies and assignments are given in Table 1. As shown in Figure 3a, the characteristic peaks located at 229.0 eV and 231.9 eV (take MoS₂/Ni₂P-38 as an example, the following is the same) can be assigned to Mo 3d_{5/2} and Mo 3d_{3/2} respectively, suggesting the existence of Mo⁴⁺. The two peaks at 232.9 eV and 236.0 eV are ascribed to the compounds MoO₃ or MoO₄²⁻ (Mo⁶⁺) due to the oxidation of the samples. In addition, the weak peak appearing at 226.4 eV corresponds to S 2s of MoS₂ [56]. For S 2p spectra, which is shown in Figure 3b, the two peaks at 161.8 eV and 163.3 eV are attributed to the 2p_{3/2} and 2p_{1/2} orbitals of divalent sulfide ion (S²⁻), while the other two peaks at 168.9 eV and 170.0 eV represent the existence of tetravalent sulfur in the form of SO₃²⁻ (S⁴⁺). Generally, the sulphur atom with a +4 state locates at the edge of MoS₂ layered structure due to the oxidation of MoS₂ particle [57].

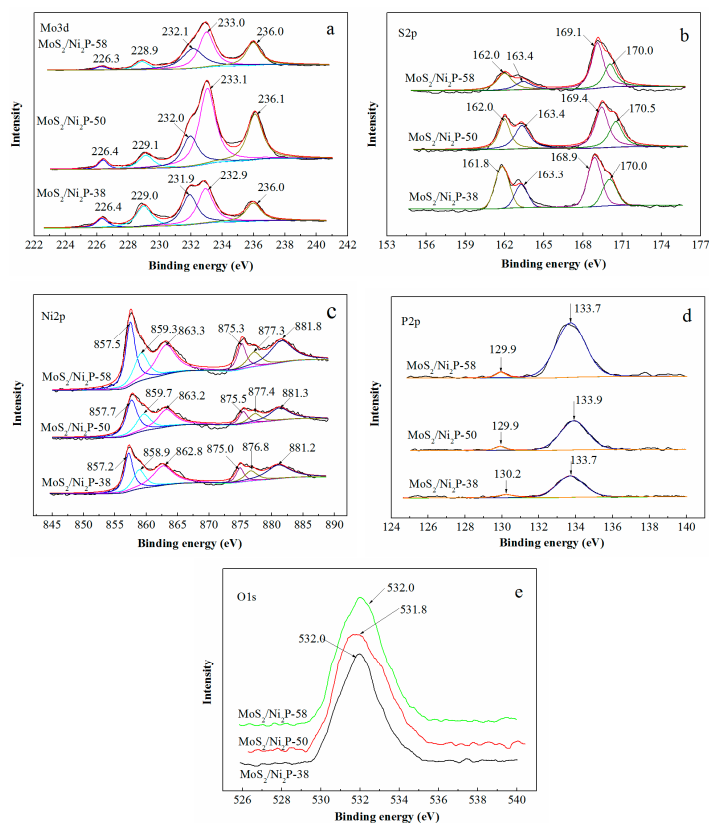


Figure 3. XPS spectra of three MoS₂/Ni₂P hybrids: (a) Mo 3d; (b) S 2p; (c) Ni 2p; (d) P 2p; and (e) O 1s.

As shown in Figure 3c, the three peaks observed at 857.2 eV, 858.9 eV and 862.8 eV may be assigned to $\text{Ni}^{\delta+}$ ($0 < \delta < 2$) in Ni_2P , oxidized Ni species (Ni^{2+}) and the satellite of $\text{Ni } 2p_{3/2}$, respectively, while the other three peaks at 875.0 eV, 876.8 eV, and 881.2 eV can be indexed to $\text{Ni}^{\delta+}$ in Ni_2P , oxidized Ni species, and the satellite of $\text{Ni } 2p_{1/2}$ [58]. As for the P 2p spectra (Figure 3d), the peak at 130.2 eV is mark of metal-P bonds in metal phosphides, the peak at 133.7 eV can be assumed to the oxidized P species because the samples are exposed to the air [59].

Additionally, the O 1s peak (Figure 3e), with the binding energies of 532.0 eV, indicates the existence of Mo(IV)-O bond [60]. Thus, to some extent, it is also confirmed that the three hybrids were oxidized during the preparation process.

Table 1. Bond energies and assignments of Mo 3d, S 2p, Ni 2p, P 2p, and O 1s photoelectron peaks of three $\text{MoS}_2/\text{Ni}_2\text{P}$ hybrids.

Bond Energies/(eV)	$\text{MoS}_2/\text{Ni}_2\text{P-38}$	$\text{MoS}_2/\text{Ni}_2\text{P-50}$	$\text{MoS}_2/\text{Ni}_2\text{P-58}$	Assignments	References
Mo 3d	229.0	229.1	228.9	Mo^{4+}	[56]
	231.9	232.0	232.1	Mo^{4+}	
	232.9	233.1	233.0	Mo^{6+}	
	236.0	236.1	236.0	Mo^{6+}	
	226.4	226.4	226.3	S 2s	
S 2p	161.8	162.0	162.0	S^{2-}	[57]
	163.3	163.4	163.4	S^{2-}	
	168.9	169.4	169.1	S^{4+}	
	170.0	170.5	170.0	S^{4+}	
Ni 2p	857.2	857.7	857.5	$\text{Ni}^{\delta+}$ ($0 < \delta < 2$)	[58]
	858.9	859.7	859.3	Ni^{2+}	
	862.8	863.2	863.3	$\text{Ni } 2p_{3/2}$	
	875.0	875.5	875.3	$\text{Ni}^{\delta+}$ ($0 < \delta < 2$)	
	876.8	877.4	877.3	Ni^{2+}	
	881.2	881.3	881.8	$\text{Ni } 2p_{1/2}$	
P 2p	130.2	129.9	129.9	Metal-P	[59]
	133.7	133.9	133.7	P-O	
O 1s	532.0	531.8	532.0	Mo(IV)-O	[60]

3.1.4. N_2 Adsorption/Desorption Isotherm Measurement

The specific surface areas of the as-synthesized pure MoS_2 , Ni_2P , and three $\text{MoS}_2/\text{Ni}_2\text{P}$ hybrids were characterized by N_2 adsorption/desorption isotherm measurement (Figure 4). All curves reveal a type IV isotherm with a distinct hysteresis loop, indicating the mesoporous structures of the above samples. The specific surface areas of aforementioned three hybrids are in a trend: $\text{MoS}_2/\text{Ni}_2\text{P-50}$ ($2.42 \text{ m}^2/\text{g}$) > $\text{MoS}_2/\text{Ni}_2\text{P-58}$ ($1.95 \text{ m}^2/\text{g}$) > $\text{MoS}_2/\text{Ni}_2\text{P-38}$ ($1.86 \text{ m}^2/\text{g}$). The specific surface areas of these three hybrids are smaller than that of pure Ni_2P ($4.62 \text{ m}^2/\text{g}$). For pure MoS_2 , although its specific surface area ($7.04 \text{ m}^2/\text{g}$) is larger than the other four samples, its basal surface is HER inert, so it cannot provide abundant active sites for hydrogen adsorption, which means an inferior HER property. Among the three hybrids, $\text{MoS}_2/\text{Ni}_2\text{P-50}$ possess the largest specific surface area, the HER performance of this hybrid will be more outstanding than the other two hybrids. However, its HER characteristic cannot be comparable to that of Ni_2P , because of its smaller determined specific surface area (ca. 52.4% of that of Ni_2P).

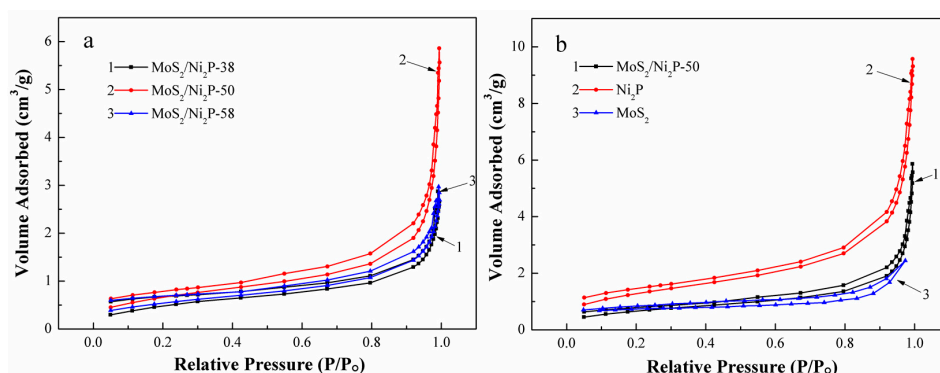


Figure 4. N_2 adsorption/desorption curves of the samples: (a) MoS_2/Ni_2P -38, MoS_2/Ni_2P -50, and MoS_2/Ni_2P -58; (b) MoS_2/Ni_2P -50, Ni_2P , and MoS_2 .

3.2. Electrochemical Analysis of HER

3.2.1. Linear Sweep Voltammetry (LSV)

The LSV curves of all samples in 1.0 mol/L KOH at a scan rate of 2 mV/s are depicted in Figure 5. The obtained onset overpotentials (η_{onset}) [61] are tabulated in Table 2. All samples were measured within the potential window of -0.8 – 0.2 V. The pure MoS_2 shows the lower HER activity which is attributed to its inert basal surface and inferior conductivity [28]. By contrast, HER performances of the three hybrids are higher than pure MoS_2 because of the excellent conductivity and affordable active sites. Although the catalytic performances of three MoS_2/Ni_2P hybrids are lower than those of Ni_2P and commercial Pt/C, they can still raise attention in hydrogen evolution reaction. When the potential was kept at -0.1 V, the cathodic current density of HER for tested samples is in the following sequence: MoS_2 (1.56 mA/cm²) < MoS_2/Ni_2P -38 (1.86 mA/cm²) < MoS_2/Ni_2P -58 (2.52 mA/cm²) < MoS_2/Ni_2P -50 (3.53 mA/cm²) < Ni_2P (5.71 mA/cm²) < Pt/C (8.57 mA/cm²). Herein, it should be mentioned that although Ni_2P shows a better HER feature than the produced three hybrids, its stability will be worse in an alkaline solution [14]. Among the three hybrids, MoS_2/Ni_2P -50 shows a high cathodic current density (70 mA/cm² at -0.48 V), thus exhibiting the best HER performance. The HER performance of this hybrid might be due to the excellent conductivity, as well as the coexistence of nanosheet-type Ni_2P crystal on the bottom and nanoflower-like MoS_2 on the surface. Without doubt, the incorporation of Ni_2P brings a great enhancement in HER performance of MoS_2 .

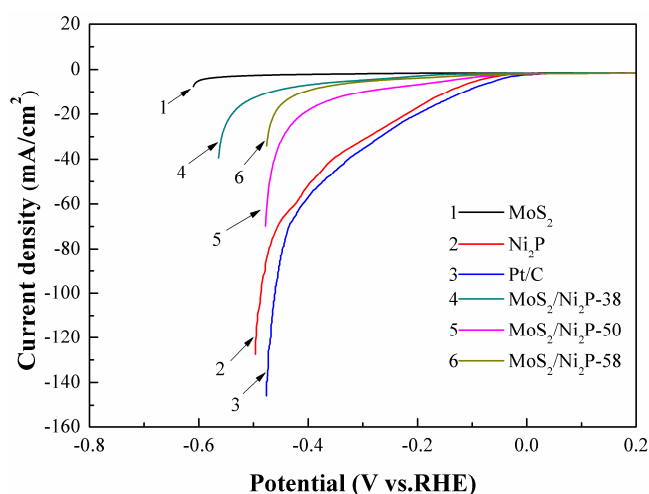


Figure 5. LSV curves of the pure MoS_2 , Ni_2P , three MoS_2/Ni_2P hybrids, and commercial 20 wt % Pt/C. Scan rate: 2 mV/s, potential window: -0.8 – 0.2 V (vs. RHE).

Table 2. The obtained values of onset overpotentials (η_{onset}), Tafel slope (b), and charge transfer coefficient (α).

Samples	$\eta_{\text{onset}} /(\text{mV})$	$b/(\text{mV/Decade})$	α
MoS ₂	−245	128	0.46
Ni ₂ P	−48	49	1.21
20 wt % Pt/C	−25	35	1.69
MoS ₂ /Ni ₂ P-38	−124	102	0.58
MoS ₂ /Ni ₂ P-50	−86	58	1.02
MoS ₂ /Ni ₂ P-58	−111	70	0.84

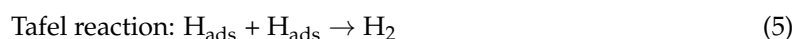
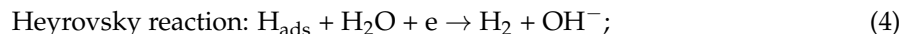
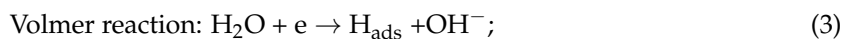
3.2.2. Tafel Polarization

Equation (1) was employed to describe the relationship of overpotential (η , V) and current density (j , mA/cm²); the charge transfer coefficient (α) can be obtained by Equation (2) [62]:

$$\eta = b \times \log j + A \quad (1)$$

$$b = \frac{2.303RT}{m_e \alpha F} \quad (2)$$

where b and R are the Tafel slope (mV/decade) and gas constant (8.314 J/(K·mol)), respectively. A is an analyzed constant, T is the absolute temperature, m_e is number of electrons transferred, and F is the Faraday constant (96,485 C/mol). According to published studies [12,13], the HER in alkaline solutions is typically considered as the Volmer-Heyrovsky process or Volmer-Tafel pathways, they are depicted as follows:



The kinetic mechanism in the HER process is determined by the rate-determining step (rds) of a multi-step reaction. The Tafel equation can play an important role in estimating the kinetic mechanism. The parameter of α corresponds to the rds for multi-step reactions, this is depicted as follows: the value of α is ~0.5 when the rds is Volmer reaction step, the value of α is ~1.5 when the rds is Heyrovsky reaction step, and the value of α will be close to 2 when the rds is step Tafel reaction [63,64]. Additionally, the Tafel slope is an important factor to describe the HER rate by examining the change of current density with overpotential. Generally, a small Tafel slope is desirable to drive a large catalytic current density at low overpotentials [65]. The Tafel plots of these samples derived from the polarization curves are shown in Figure 6. The HER performance of MoS₂ is inferior due to its large Tafel slope (~128 mV/decade) and small α (0.46). Within three MoS₂/Ni₂P hybrids, MoS₂/Ni₂P-50 has a minimum Tafel slope (~58 mV/decade), indicative of the excellent HER performance. It might be a substitute to noble metals in HER application.

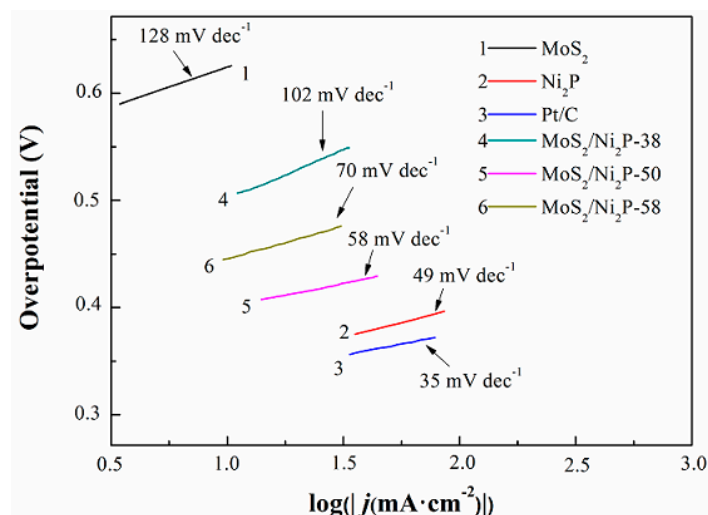


Figure 6. Tafel plots of MoS₂, Ni₂P, three MoS₂/Ni₂P hybrids, and commercial 20 wt % Pt/C. Scan rate: 2 mV/s, potential window: 0.3~0.65 V.

3.2.3. Cyclic Voltammetry (CV)

Cyclic voltammetry (CV) measurement (in a potential window of $-0.6\sim 0.8$ V) can be helpful to reveal the reversibility of the electrochemical reaction. CV curves of MoS₂/Ni₂P-38, MoS₂/Ni₂P-50 and MoS₂/Ni₂P-58 samples are exhibited in Figure 7; the inset shows those of MoS₂/Ni₂P-50, pure MoS₂, pure Ni₂P and Pt/C. It can be seen from the determined CV curves that each of them is composed of an anodic oxidation and a cathodic reduction peak. The quasi-reversible redox peaks may be related to the processes of electrochemical hydrogen adsorption and electrochemical hydrogen desorption [28]. For the three hybrids, cathodic reduction potentials of them are as follows: -0.21 V for MoS₂/Ni₂P-38, -0.11 V for MoS₂/Ni₂P-50, and -0.15 V for MoS₂/Ni₂P-58. In addition, the current density follows the same tendency. Thus, a positive potential and the large current density for MoS₂/Ni₂P-50 composite can be validated, inferring its higher HER property than those of the other two hybrids.

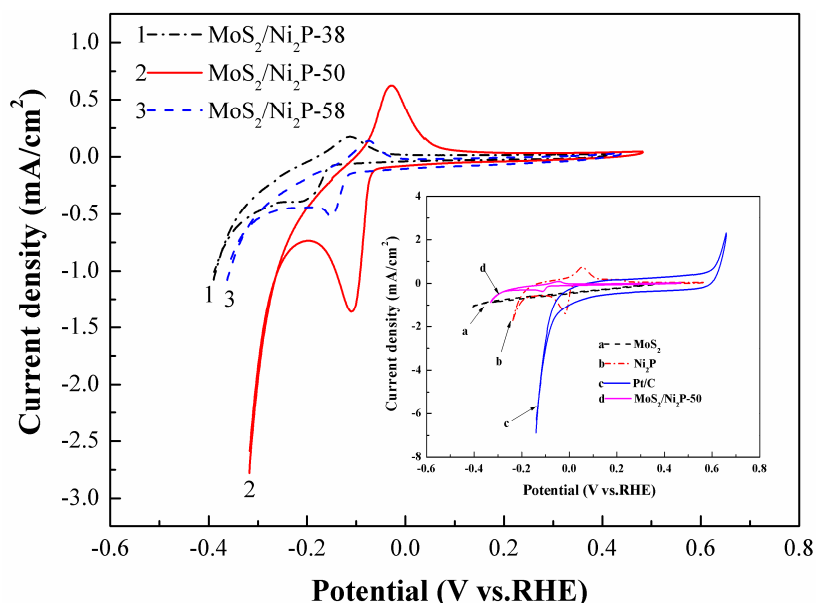


Figure 7. CV curves of pure MoS₂, Ni₂P, three MoS₂/Ni₂P hybrids and commercial 20 wt % Pt/C. Scan rate: 10 mV/s, potential window: $-0.6\sim 0.8$ V (vs. RHE).

3.2.4. Electrochemical Impedance Spectroscopy (EIS)

The obtained Nyquist plots for the pure MoS₂, Ni₂P and three MoS₂/Ni₂P samples are shown in Figure 8. The R_s (CPE/R_{ct}) equivalent circuit was adopted to analyze the obtained EIS data by use of Zsimpwin software. Where R_s (Ω·cm²) and R_{ct} (kΩ·cm²) are the solution resistance and charge transfer resistance. The double layer capacitance (C_{dl}) and the exchange current density (j₀) of the electrode are calculated by Equations (6) and (7) [6,66,67]:

$$C_{dl} = \left[\frac{Q}{(R_s^{-1} + R_{ct}^{-1})^{1-n}} \right]^{\frac{1}{n}} \quad (6)$$

$$j_0 = \frac{RT}{m_e F R_{ct}} \quad (7)$$

Herein, Q is the capacitance coefficient (Ω⁻¹·sⁿ·cm⁻²) of constant phase element (CPE), and n is the phase angle of constant phase element. R is the gas constant (J/(K·mol)), T is the absolute temperature (K), m_e is the number of switched electrons (the parameter of m_e is the same as that in Equation (2)) and F is the Faraday constant. The calculated values of them are also reported in Table 3.

Of all the tested samples, it is no doubt that Pt/C, with the feature of the largest C_{dl} and j₀, exhibits the best HER performance. Apart from the commercial Pt/C specimen, among other five lab-made samples, pure Ni₂P has the largest C_{dl} and j₀, followed by the three hybrids and, lastly, by the pure MoS₂. From the above results, it seems that Ni₂P is an ideal HER catalyst, however, the demerit of its instability in alkaline solution will retard its application. Although C_{dl} and j₀ of the three hybrids are smaller than Ni₂P, they are much larger than that of MoS₂. Among these catalysts, the HER performance of MoS₂/Ni₂P-50 is remarkable.

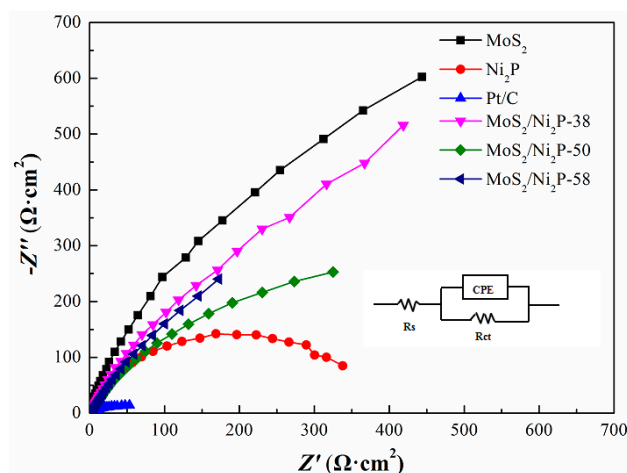


Figure 8. EIS spectra of pure MoS₂, Ni₂P, three MoS₂/Ni₂P hybrids, and commercial 20 wt % Pt/C. Cathodic overpotential: 0.7 V, frequency: 10⁵ Hz–0.01 Hz, amplitude of the sinusoidal signal: 5 mV.

Table 3. Parameters of solution resistance (R_s), charge transfer resistance (R_{ct}), double-layer capacitance (C_{dl}), the dimensionless CPE exponent n, and exchange current density (j₀) analyzed from the EIS spectra.

Samples	R _s /(Ω·cm ²)	R _{ct} /(kΩ·cm ²)	n	C _{dl} /(×10 ⁻⁵ ·F/cm ²)	j ₀ /(×10 ⁻⁵ ·A/cm ²)
MoS ₂	0.66	55.6	0.844	0.726	0.02
Ni ₂ P	0.74	0.41	0.793	7.452	3.11
20 wt % Pt/C	2.27	0.056	0.670	51.306	22.90
MoS ₂ /Ni ₂ P-38	0.73	2.01	0.816	1.864	0.64
MoS ₂ /Ni ₂ P-50	0.75	0.83	0.784	6.246	1.55
MoS ₂ /Ni ₂ P-58	0.71	1.82	0.837	2.614	0.71

3.3. DFT Calculations

The optimized structures of the three catalysts of MoS₂, Ni₂P, and MoS₂/Ni₂P without hydrogen adsorption, as well as those with one and two adsorbed hydrogen atoms are shown in Figure 9. The adsorption energy (ΔE_{ads}) and Gibbs free energy of adsorption (ΔG_{ads}) for the uptake of hydrogen by the catalyst at 298 K were calculated using Equations (8) and (9) [30].

$$\Delta E_{\text{ads}} = E(\text{catalyst} + x\text{H}) - E(\text{catalyst} + (x - 1)\text{H}) - \frac{1}{2}E(\text{H}_2) \quad (8)$$

$$\Delta G_{\text{ads}} = \Delta E_{\text{ads}} + G_{298}(\text{catalyst} + x\text{H}) - G_{298}(\text{catalyst} + (x - 1)\text{H}) - \frac{1}{2}G_{298}(\text{H}_2) \quad (9)$$

where $E(\text{catalyst} + x\text{H}, x = 1 \text{ or } 2)$ is the COSMO-corrected total energy for the system containing the catalyst support and x adsorbed hydrogen atoms, $E(\text{catalyst} + (x - 1)\text{H})$ is that of for $(x - 1)$ adsorbed hydrogen atoms-including system, and $E(\text{H}_2)$ is the energy of an isolated hydrogen molecule. $G(X)$ is the computed temperature-corrected free energy of the aforesaid species (X) at 298 K. ΔE_{ads} shows the absorption capability catalyst toward the hydrogen atom; the more negative value of ΔE_{ads} suggests the stronger interaction between them, and the geometry with the most negative ΔE_{ads} will be more stable. The negative value of ΔG_{ads} convinces the spontaneous characteristic of the adsorption interaction process.

As for pristine MoS₂, there are six edge sites (identified by numbers in Figure 9a) that can absorb the hydrogen atom. After one hydrogen atom capture, $\Delta E_{\text{ads}}(\text{MoS}_2 + \text{H})$ values are as follows: -16.12 kcal/mol for site 1, -16.07 for site 2, -16.08 for site 3, -12.91 for site 4, -12.98 for site 5, and -12.97 kcal/mol for site 6. Therefore, among these six sites, site 1 is more suitable than others for the anchor of hydrogen atom (Figure 9b). When one hydrogen atom is absorbed, the negative ΔG_{ads} of all six hydrogen-containing configurations (-13.47 , -13.34 , -13.35 , -9.55 , -9.67 , and -9.61 kcal/mol for hydrogen atom at sites 1–6) indicates the spontaneous characteristic of the hydrogen uptake. After one hydrogen atom adsorption, there are only five edge sites (2–6) for trapping another hydrogen atom. Among geometries for the two hydrogen atoms, the structure with ΔE_{ads} of -14.78 kcal/mol for MoS₂ with sites 1 and 3 for the capture of hydrogen atoms (Figure 9c) is most stable; ΔE_{ads} for others are: -13.52 kcal/mol for sites 1 and 2, -2.45 kcal/mol for sites 1 and 4, -12.37 kcal/mol for sites 1 and 5, and -13.19 kcal/mol for sites 1 and 6. The values of ΔG_{ads} of these five compounds are negative, also inferring the easy uptake of the second hydrogen atom. Of course, by comparison of ΔE_{ads} , the capture of the first hydrogen atom is easier than that of the second one.

For the case of hydrogen adsorption by Ni₂P, all four sites (labeled by numbers in Figure 9d) are employed to trap hydrogen atoms. Site 3 is desirable for the capture of the first hydrogen atom (Figure 9e), and the value ΔE_{ads} for the hydrogen-capturing compound is -6.095 kcal/mol; those for the other three compounds are -1.658 kcal/mol at site 1, -4.889 kcal/mol at site 2, and -4.898 kcal/mol at site 4. Values of ΔG_{ads} for hydrogen trapper at sites 1–4 are -0.235 kcal/mol, -4.037 kcal/mol, -4.045 kcal/mol and -4.036 kcal/mol, respectively. As for the three systems containing two hydrogens, ΔE_{ads} and ΔG_{ads} of them are -0.31 and 1.74 kcal/mol for sites 3 and 1, 1.78 and 0.33 kcal/mol for sites 3 and 2, and -4.19 and -2.23 kcal/mol for sites 3 and 4. Therefore, the Ni₂P catalyst tends to use sites 3 and 4 to trap hydrogen atoms (Figure 9f).

Lastly, for the hydrogen capture by the MoS₂/Ni₂P hybrid, among the six edge sites of top MoS₂ layer (Figure 9g), which is dissimilar to that of the pure MoS₂, site 5 is more competent for trapping the first hydrogen atom (Figure 9h), in view of ΔE_{ads} and ΔG_{ads} as follows: -4.79 and -3.57 kcal/mol for site 1, 9.15 and 11.25 kcal/mol for site 2, -4.89 and -4.83 kcal/mol for site 3, -4.99 and -4.64 kcal/mol for site 4, -6.78 and -8.36 kcal/mol for site 5, and -5.2 and -6.87 kcal/mol for site 6. Additionally, for the adsorption of two hydrogen atoms, sites 5 and 3 (Figure 9i) are the most acceptable, because of the following values of ΔE_{ads} and ΔG_{ads} for the second hydrogen uptake: -3.81 and -1.88 kcal/mol for site 1, -3.56 and -1.77 kcal/mol for site 2, -6.30 and -2.73 kcal/mol for site 3, -6.29 and -2.58 kcal/mol for site 4, 7.32 and 11.90 kcal/mol for site 6. Furthermore, it should be

mentioned that for S atoms at the sites 4 and 6, the distances between which and the second hydrogen atom are extended, and this hydrogen atom tends to close to the S atoms at sites 3 and 5.

In terms of the DFT calculations results, for the first and second hydrogen uptakes, ΔE_{ads} and ΔG_{ads} of MoS_2 are the most negative, followed by $\text{MoS}_2/\text{Ni}_2\text{P}$ and Ni_2P . Compared with that of MoS_2 , affinities of $\text{MoS}_2/\text{Ni}_2\text{P}$ and Ni_2P to hydrogen neither too strong nor too weak, indicating its excellent HER performance [51,68]. In addition, the ΔG_{ads} of Ni_2P that capturing hydrogen atoms is more close to zero than those of the other two systems, it is sure that the HER property of Ni_2P is higher than those of MoS_2 and $\text{MoS}_2/\text{Ni}_2\text{P}$ hybrids [51,69]. Thus, it can be concluded that the HER performances for these catalysts are in an order of $\text{Ni}_2\text{P} > \text{MoS}_2/\text{Ni}_2\text{P} > \text{MoS}_2$. This deduction is consistent with the experimental tests. Herein, the combination between MoS_2 and Ni_2P , and the role of Ni_2P in the enhancement of MoS_2 HER property will be investigated in a further study.

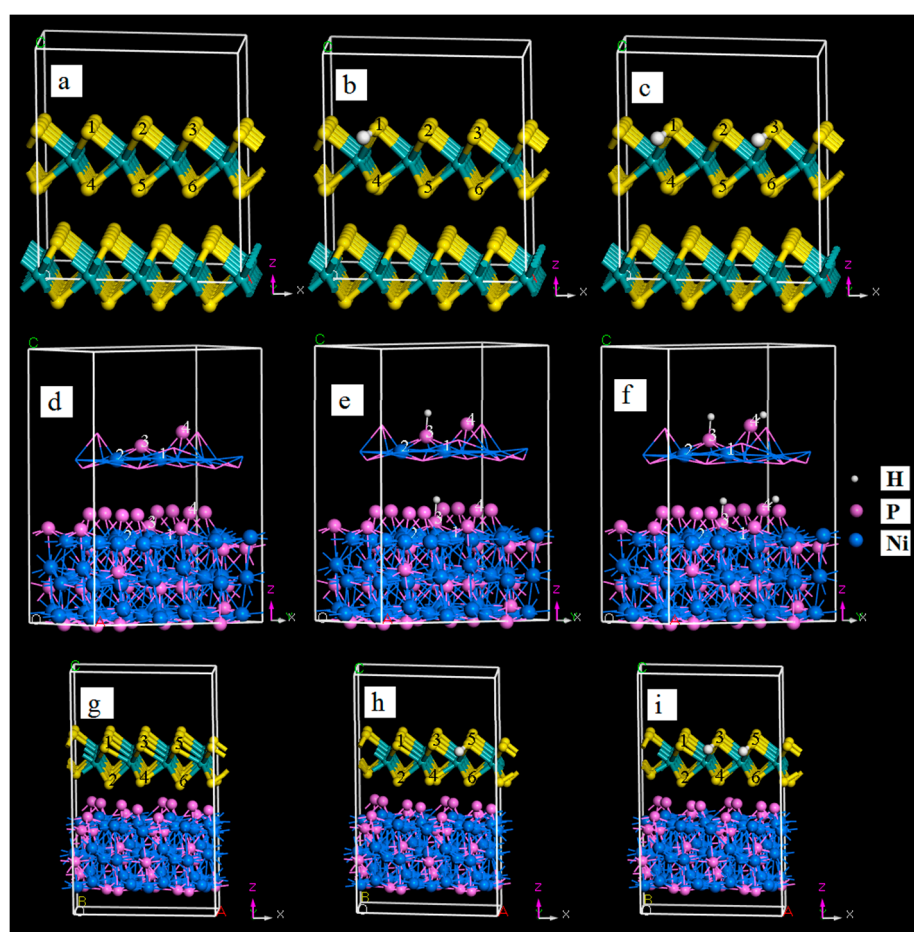


Figure 9. The optimized structures of MoS_2 , Ni_2P , and $\text{MoS}_2/\text{Ni}_2\text{P}$ three catalysts without hydrogen adsorption, as well as those with one and two adsorbed hydrogen atoms. (a) MoS_2 ; (b) $\text{MoS}_2\text{-1H}$; (c) $\text{MoS}_2\text{-2H}$; (d) Ni_2P ; (e) $\text{Ni}_2\text{P-1H}$; (f) $\text{Ni}_2\text{P-2H}$; (g) $\text{MoS}_2/\text{Ni}_2\text{P}$; (h) $\text{MoS}_2/\text{Ni}_2\text{P-1H}$; and (i) $\text{MoS}_2/\text{Ni}_2\text{P-2H}$.

3.4. HER Stability of the $\text{MoS}_2/\text{Ni}_2\text{P}$ Hybrids

For practical applications, in addition to the HER activity mentioned above, the stability of electrocatalysts is another important criterion to evaluate the catalytic activity. To assess the durability of pure MoS_2 , Ni_2P , and the $\text{MoS}_2/\text{Ni}_2\text{P-50}$ hybrid, continuous CV tests for 1000 cycles with the potential in range of -1.0 to 0.4 V were conducted at a scan rate of 50 mV/s in 1.0 mol/L KOH (Figure 10). By comparison of polarization curves of these three samples before and after 1000 cycles, the cathodic current densities of them decrease somewhat after tests. Compared with electrocatalytic

behaviors of pure MoS₂ and Ni₂P, the MoS₂/Ni₂P-50 hybrid just shows a slight decay, and thereby exhibits an excellent durability in the HER process.

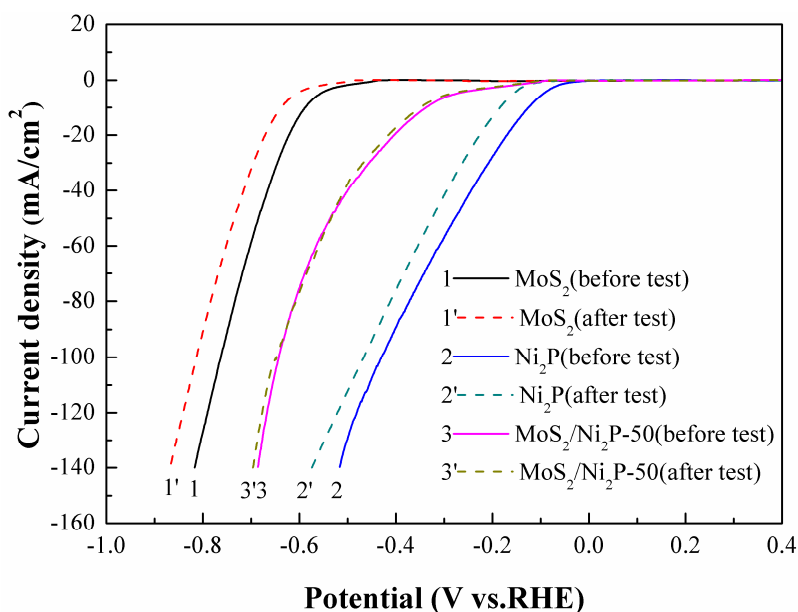


Figure 10. Stability tests for the pure MoS₂, Ni₂P, and MoS₂/Ni₂P-50 hybrid. Scan rate: 50 mV/s, potential window: −1.0 to 0.4 V (vs. RHE).

4. Conclusions

In this work, morphologies, crystallinities, and chemical components of pure MoS₂, Ni₂P, and three MoS₂/Ni₂P hybrids obtained via a hydrothermal synthesis process were characterized. Then, HER performances of them in 1.0 mol/L KOH solution were evaluated. The main conclusions are summarized as follows:

- (1) The result of DFT calculation is in consistence with that of experimental test. The incorporated Ni₂P observably enhances the HER property of MoS₂. Among the three fabricated kinds of catalysts, the HER performance of them follows the trend: Ni₂P > MoS₂/Ni₂P > MoS₂.
- (2) The MoS₂/Ni₂P-50 shows a large cathodic current density (70 mA/cm² at −0.48 V) and small Tafel slope (~58 mV/decade), thus exhibiting the higher HER activity than other two MoS₂/Ni₂P hybrids.
- (3) The excellent HER performance of MoS₂/Ni₂P-50 hybrid can be due to the desirable conductivity, the uniform morphology, large specific surface area, and favorable stability.

Author Contributions: F.Y. and N.K. prepared the manuscript. L.S. designed this work and gave the guidance for HER evaluation. F.Y., J.Y., N.K., and S.H. performed the experiments and the measurement of HER. J.H., X.W., and F.Y. analyzed the data and reviewed the manuscript. All authors read and approved the manuscript.

Funding: This research was funded by the Hebei Provincial Natural Science Foundation of China (grant number B2016203012), and the Science and Technology Support Key Research and Development Program of Qinhuangdao, China (grant number 201703A012).

Acknowledgments: We are sincerely thankful to the editors and the reviewers for giving valuable and instructive comments for the revision of this manuscript.

Conflicts of Interest: The authors declare no conflict of interest.

References

1. Han, L.; Yu, T.W.; Lei, W.; Liu, W.W.; Feng, K.; Ding, Y.L.; Jiang, G.P.; Xu, P.; Chen, Z.W. Nitrogen-doped carbon nanocones encapsulating with nickel–cobalt mixed phosphides for enhanced hydrogen evolution reaction. *J. Mater. Chem. A* **2017**, *5*, 16568–16572. [[CrossRef](#)]
2. Li, Y.; Cai, P.W.; Ci, S.Q.; Wen, Z.H. Strongly coupled 3D nanohybrids with Ni₂P/carbon nanosheets as pH-universal hydrogen evolution reaction electrocatalysts. *ChemElectroChem* **2017**, *4*, 340–344. [[CrossRef](#)]
3. Li, J.Y.; Li, J.; Zhou, X.M.; Xia, Z.M.; Gao, W.; Qu, Y.Q. Highly efficient and robust nickel phosphides as bifunctional electrocatalysts for overall water-splitting. *ACS Appl. Mater. Interfaces* **2016**, *8*, 10826–10834. [[CrossRef](#)] [[PubMed](#)]
4. Song, L.Z.; Wang, X.L.; Wen, F.S.; Niu, L.J.; Shi, X.M.; Yan, J.Y. Hydrogen evolution reaction performance of the molybdenum disulfide/nickel–phosphorus composites in alkaline solution. *Int. J. Hydrog. Energy* **2016**, *41*, 18942–18952. [[CrossRef](#)]
5. Wang, D.Z.; Pan, Z.; Wu, Z.Z.; Wang, Z.P.; Liu, Z.H. Hydrothermal synthesis of MoS₂ nanoflowers as highly efficient hydrogen evolution reaction catalysts. *J. Power Sources* **2014**, *264*, 229–234. [[CrossRef](#)]
6. Wang, L.X.; Li, Y.; Yin, X.C.; Wang, Y.Z.; Lu, L.; Song, A.L.; Xia, M.R.; Li, Z.P.; Qin, X.J.; Shao, G.J. Comparison of three nickel-based carbon composite catalysts for hydrogen evolution reaction in alkaline solution. *Int. J. Hydrog. Energy* **2017**, *42*, 22655–22662. [[CrossRef](#)]
7. Cai, Z.X.; Song, X.H.; Wang, Y.R.; Chen, X. Electrodeposition-assisted synthesis of Ni₂P nanosheets on 3D graphene/Ni foam electrode and its performance for electrocatalytic hydrogen production. *ChemElectroChem* **2015**, *2*, 1665–1671. [[CrossRef](#)]
8. Morales-Guio, C.G.; Stern, L.A.; Hu, X. Nanostructured hydrotreating catalysts for electrochemical hydrogen evolution. *Chem. Soc. Rev.* **2014**, *43*, 6555–6569. [[CrossRef](#)] [[PubMed](#)]
9. Merki, D.; Hu, X. Recent developments of molybdenum and tungsten sulfides as hydrogen evolution catalysts. *Energy Environ. Sci.* **2011**, *4*, 3878–3888. [[CrossRef](#)]
10. Khan, M.; Yousaf, A.B.; Chen, M.M.; Wei, C.S.; Wu, X.; Huang, N.D.; Qi, Z.M.; Li, L.B. Molybdenum sulfide/graphene-carbon nanotube nanocomposite material for electrocatalytic applications in hydrogen evolution reactions. *Nano Res.* **2016**, *9*, 837–848. [[CrossRef](#)]
11. Jing, S.Y.; Zhang, L.S.; Luo, L.; Lu, J.J.; Yin, S.B.; Shen, P.K.; Tsiakaras, P. N-doped porous molybdenum carbide nanobelts as efficient catalysts for hydrogen evolution reaction. *Appl. Catal. B Environ.* **2018**, *224*, 533–540. [[CrossRef](#)]
12. Yin, X.C.; Sun, G.; Song, A.L.; Wang, L.X.; Wang, Y.Z.; Dong, H.F.; Shao, G.J. A novel structure of Ni–(MoS₂/GO) composite coatings deposited on Ni foam under supergravity field as efficient hydrogen evolution reaction catalysts in alkaline solution. *Electrochim. Acta* **2017**, *249*, 52–63. [[CrossRef](#)]
13. Yin, X.C.; Sun, G.; Wang, L.X.; Bai, L.; Su, L.; Wang, Y.Z.; Du, Q.H.; Shao, G.J. 3D hierarchical network NiCo₂S₄ nanoflakes grown on Ni foam as efficient bifunctional electrocatalysts for both hydrogen and oxygen evolution reaction in alkaline solution. *Int. J. Hydrog. Energy* **2017**, *42*, 25267–25276. [[CrossRef](#)]
14. Popczun, E.J.; McKone, J.R.; Read, C.G.; Biacchi, A.J.; Wiltrout, A.M.; Lewis, N.S.; Schaak, R.E. Nanostructured nickel phosphide as an electrocatalyst for the hydrogen evolution reaction. *J. Am. Chem. Soc.* **2013**, *135*, 9267–9270. [[CrossRef](#)] [[PubMed](#)]
15. Feng, L.G.; Vrabel, H.; Bensimon, M.; Hu, X. Easily-prepared dinickel phosphide (Ni₂P) nanoparticles as an efficient and robust electrocatalyst for hydrogen evolution. *Phys. Chem. Chem. Phys.* **2014**, *16*, 5917–5921. [[CrossRef](#)] [[PubMed](#)]
16. Liu, Y.R.; Hu, W.H.; Li, X.; Dong, B.; Shang, X.; Han, G.Q.; Chai, Y.M.; Liu, Y.Q.; Liu, C.G. One-pot synthesis of hierarchical Ni₂P/MoS₂ hybrid electrocatalysts with enhanced activity for hydrogen evolution reaction. *Appl. Surf. Sci.* **2016**, *383*, 276–282. [[CrossRef](#)]
17. Pan, Y.; Yang, N.; Chen, Y.J.; Lin, Y.; Li, Y.P.; Liu, Y.Q.; Liu, C.G. Nickel phosphide nanoparticles-nitrogen-doped graphene hybrid as an efficient catalyst for enhanced hydrogen evolution activity. *J. Power Sources* **2015**, *297*, 45–52. [[CrossRef](#)]
18. Lu, G.J.; Evans, P.; Zangari, G. Electrocatalytic properties of Ni-based alloys toward hydrogen evolution reaction in acid media. *J. Electrochem. Soc.* **2003**, *150*, A551–A557. [[CrossRef](#)]

19. Peng, S.G.; Li, L.L.; Han, X.P.; Sun, W.P.; Srinivasan, M.; Mhaisalkar, S.G.; Cheng, F.Y.; Yan, Q.Y.; Chen, J.; Ramakrishna, S. Cobalt sulfide nanosheet/graphene/carbon nanotube nanocomposites as flexible electrodes for hydrogen evolution. *Angew. Chem.* **2014**, *53*, 12594–12599.
20. Zhang, H.X.; Yang, B.; Wu, X.L.; Li, Z.J.; Lei, L.C.; Zhang, X.W. Polymorphic CoSe₂ with mixed orthorhombic and cubic phases for highly efficient hydrogen evolution reaction. *ACS Appl. Mater. Interfaces* **2015**, *7*, 1772–1779. [[CrossRef](#)] [[PubMed](#)]
21. Li, Y.H.; Liu, P.F.; Pan, L.F.; Wang, H.F.; Yang, Z.Z.; Zheng, L.R.; Hu, P.; Zhao, H.J.; Gu, L.; Yang, H.G. Local atomic structure modulations activate metal oxide as electrocatalyst for hydrogen evolution in acidic water. *Nat. Commun.* **2015**, *6*, 8064. [[CrossRef](#)] [[PubMed](#)]
22. Chen, W.F.; Wang, C.H.; Sasaki, K.; Marinkovic, N.; Xu, W.; Muckerman, J.T.; Zhu, Y.; Adzic, R.R. Highly active and durable nanostructured molybdenum carbide electrocatalysts for hydrogen production. *Energy Environ. Sci.* **2013**, *6*, 943–951. [[CrossRef](#)]
23. Chen, W.F.; Sasaki, K.; Ma, C.; Frenkel, A.I.; Marinkovic, N.; Muckerman, J.T.; Zhu, Y.M.; Adzic, R.R. Hydrogen-evolution catalysts based on non-noble metal nickel–molybdenum nitride nanosheets. *Angew. Chem. Int. Ed.* **2012**, *51*, 6131–6135. [[CrossRef](#)] [[PubMed](#)]
24. Du, H.F.; Gu, S.; Liu, R.W.; Li, C.M. Highly active and inexpensive iron phosphide nanorods electrocatalyst towards hydrogen evolution reaction. *Int. J. Hydrog. Energy* **2015**, *40*, 14272–14278. [[CrossRef](#)]
25. Kibsgaard, J.; Chen, Z.B.; Reinecke, B.N.; Jaramillo, T.F. Engineering the surface structure of MoS₂ to preferentially expose active edge sites for electrocatalysis. *Nat. Mater.* **2012**, *11*, 963–969. [[CrossRef](#)] [[PubMed](#)]
26. Merki, D.; Fierro, S.; Vrabel, H.; Hu, X.L. Amorphous molybdenum sulfide films as catalysts for electrochemical hydrogen production in water. *Chem. Sci.* **2011**, *2*, 1262–1267. [[CrossRef](#)]
27. Liu, Y.R.; Hu, W.H.; Li, X.; Dong, B.; Shang, X.; Han, G.Q.; Chai, Y.M.; Liu, Y.Q.; Liu, C.G. Facile one-pot synthesis of CoS₂–MoS₂/CNTs as efficient electrocatalyst for hydrogen evolution reaction. *Appl. Surf. Sci.* **2016**, *384*, 51–57. [[CrossRef](#)]
28. He, J.; Song, L.Z.; Yan, J.Y.; Kang, N.; Zhang, Y.L.; Wang, W. Hydrogen evolution reaction property in alkaline solution of molybdenum disulfide modified by surface anchor of Nickel–Phosphorus coating. *Metals* **2017**, *7*, 211.
29. Bian, X.J.; Zhu, J.; Liao, L.; Scanlon, M.D.; Ge, P.Y.; Ji, C.; Girault, H.H.; Liu, B.H. Nanocomposite of MoS₂ on ordered mesoporous carbon Nanospheres: A highly active catalyst for electrochemical hydrogen evolution. *Electrochem. Commun.* **2012**, *22*, 128–132. [[CrossRef](#)]
30. Tsai, C.; Abild-Pedersen, F.; Nørskov, J.K. Tuning the MoS₂ edge-site activity for hydrogen evolution via support interactions. *Nano Lett.* **2014**, *14*, 1381–1387. [[CrossRef](#)] [[PubMed](#)]
31. Jing, Y.; Ortiz-Quiles, E.O.; Cabrera, C.R.; Chen, Z.F.; Zhou, Z. Layer-by-layer hybrids of MoS₂ and reduced graphene oxide for lithium ion batteries. *Electrochim. Acta* **2014**, *147*, 392–400. [[CrossRef](#)]
32. Yu, Y.F.; Huang, S.Y.; Li, Y.P.; Steinmann, S.N.; Yang, W.T.; Cao, L.Y. Layer-dependent electrocatalysis of MoS₂ for hydrogen evolution. *Nano Lett.* **2014**, *14*, 553–558. [[CrossRef](#)] [[PubMed](#)]
33. Liang, T.; Sawyer, W.G.; Perry, S.S.; Sinnott, S.B.; Phillpot, S.R. Energetics of oxidation in MoS₂ nanoparticles by density functional theory. *J. Phys. Chem. C* **2011**, *115*, 10606–10616. [[CrossRef](#)]
34. Wu, Z.Z.; Fang, B.Z.; Wang, Z.P.; Wang, C.L.; Liu, Z.H.; Liu, F.Y.; Wang, W.; Alfantazi, A.; Wang, D.Z.; Wilkinson, D.P. MoS₂ nanosheets: A designed structure with high active site density for the hydrogen evolution reaction. *ACS Catal.* **2013**, *3*, 2101–2107. [[CrossRef](#)]
35. Wang, H.T.; Lu, Z.Y.; Kong, D.S.; Sun, J.; Hymel, T.M.; Cui, Y. Electrochemical tuning of MoS₂ nanoparticles on three-dimensional substrate for efficient hydrogen evolution. *ACS Nano* **2014**, *8*, 4940–4947. [[CrossRef](#)] [[PubMed](#)]
36. Deng, J.; Li, H.B.; Xiao, J.P.; Tu, Y.C.; Deng, D.H.; Yang, H.X.; Tian, H.F.; Li, J.Q.; Ren, P.J.; Bao, X.H. Triggering the electrocatalytic hydrogen evolution activity of inert two-dimensional MoS₂ surface via single-atom metal doping. *Energy Environ. Sci.* **2015**, *8*, 1594–1601. [[CrossRef](#)]
37. Huang, X.; Zeng, Z.Y.; Bao, S.Y.; Wang, M.F.; Qi, X.Y.; Fan, Z.X.; Zhang, H. Solution-phase epitaxial growth of noble metal nanostructures on dispersible single-layer molybdenum disulfide nanosheets. *Nat. Commun.* **2013**, *4*, 1444–1452. [[CrossRef](#)] [[PubMed](#)]

38. Hu, W.H.; Han, G.Q.; Liu, Y.R.; Dong, B.; Chai, Y.M.; Liu, Y.Q.; Liu, C.G. Ultrathin MoS₂-coated carbon nanospheres as highly efficient electrocatalysts for hydrogen evolution reaction. *Int. J. Hydrog. Energy* **2015**, *40*, 6552–6558. [[CrossRef](#)]
39. Chen, Z.B.; Cummins, D.; Reinecke, B.N.; Clark, E.; Sunkara, M.K.; Jaramillo, T.F. Core-shell MoO₃-MoS₂ nanowires for hydrogen evolution: A functional design for electrocatalytic materials. *Nano Lett.* **2011**, *11*, 4168–4175. [[CrossRef](#)] [[PubMed](#)]
40. Sun, X.; Huo, J.; Yang, Y.D.; Xu, L.; Wang, S.Y. The Co₃O₄ nanosheet array as support for MoS₂ as highly efficient electrocatalysts for hydrogen evolution reaction. *J. Energy Chem.* **2017**, *26*, 1136–1139. [[CrossRef](#)]
41. Li, Y.G.; Wang, H.L.; Xie, L.M.; Liang, Y.Y.; Hong, G.S.; Dai, H.J. MoS₂ nanoparticles grown on Graphene: An advanced catalyst for the hydrogen evolution reaction. *J. Am. Chem. Soc.* **2011**, *133*, 7296–7299. [[CrossRef](#)] [[PubMed](#)]
42. Li, X.D.; Yu, S.; Wu, S.Q.; Wen, Y.H.; Zhou, S.; Zhu, Z.Z. Structural and electronic properties of superlattice composed of graphene and monolayer MoS₂. *J. Phys. Chem. C* **2013**, *117*, 15347–15353. [[CrossRef](#)]
43. Zhang, J.M.; Zhao, L.; Liu, A.P.; Li, X.Y.; Wu, H.P.; Lu, C.D. Three-dimensional MoS₂/rGO hydrogel with extremely high double-layer capacitance as active catalyst for hydrogen evolution reaction. *Electrochim. Acta* **2015**, *182*, 652–658. [[CrossRef](#)]
44. Paseka, I. Hydrogen evolution reaction on Ni–P alloys: The internal stress and the activities of electrodes. *Electrochim. Acta* **2008**, *53*, 4537–4543. [[CrossRef](#)]
45. Liu, Q.; Gu, S.; Li, C.M. Electrodeposition of Nickel–Phosphorus nanoparticles film as a Janus electrocatalyst for electro-splitting of water. *J. Power Sources* **2015**, *299*, 342–346. [[CrossRef](#)]
46. Balaraju, J.N.; Jahan, S.M.; Jain, A.; Rajama, K.S. Structure and phase transformation behavior of electrodeless Ni–P alloys containing tin and tungsten. *J. Alloys Compd.* **2007**, *436*, 319–327. [[CrossRef](#)]
47. Pu, Z.H.; Liu, Q.; Tang, C.; Asiri, A.M.; Sun, X.P. Ni₂P nanoparticle films supported on a Ti plate as an efficient hydrogen evolution cathode. *Nanoscale* **2014**, *6*, 11031–11034. [[CrossRef](#)] [[PubMed](#)]
48. Raybaud, P.; Hafner, J.; Kresse, G.; Kasztelan, S.; Toulhoat, H. Ab initio study of the H₂-H₂S/MoS₂ gas-solid Interface: The nature of the catalytically active sites. *J. Catal.* **2000**, *189*, 129–146. [[CrossRef](#)]
49. Ouyang, F.P.; Yang, Z.X.; Ni, X.; Wu, N.N.; Chen, Y.; Xiong, X. Hydrogenation-induced edge magnetization in armchair MoS₂ nanoribbon and electric field effects. *Appl. Phys. Lett.* **2014**, *104*, 071901. [[CrossRef](#)]
50. Moon, J.S.; Jang, J.H.; Kim, E.G.; Chung, Y.H.; Yoo, S.J.; Lee, Y.K. The nature of active sites of Ni₂P electrocatalyst for hydrogen evolution reaction. *J. Catal.* **2015**, *326*, 92–99. [[CrossRef](#)]
51. Liu, P.; Rodriguez, J.A. Catalysts for hydrogen evolution from the [NiFe] hydrogenase to the Ni₂P (001) surface: The importance of ensemble effect. *J. Am. Chem. Soc.* **2005**, *127*, 14871–14878. [[CrossRef](#)] [[PubMed](#)]
52. Wang, X.L.; Song, L.Z.; Yang, F.F.; He, J. Investigation of phosphate adsorption by a polyethersulfone-type affinity membrane using experimental and DFT methods. *Desalin. Water Treat.* **2016**, *57*, 25036–25056. [[CrossRef](#)]
53. Li, H.; Ma, L.; Chen, W.X.; Wang, J.M. Synthesis of MoS₂/C nanocomposites by hydrothermal route used as Li-ion intercalation electrode materials. *Mater. Lett.* **2009**, *63*, 1363–1365. [[CrossRef](#)]
54. Li, D.; Senevirathne, K.; Aquilina, L.; Brock, S.L. Effect of synthetic levers on nickel phosphide nanoparticle formation: Ni₅P₄ and NiP₂. *Inorg. Chem.* **2015**, *54*, 7968–7975. [[CrossRef](#)] [[PubMed](#)]
55. Liu, Z.Y.; Huang, X.; Zhu, Z.B.; Dai, J.H. A simple mild hydrothermal route for the synthesis of nickel phosphide powders. *Ceram. Int.* **2010**, *36*, 1155–1158. [[CrossRef](#)]
56. Wang, H.W.; Skeldon, P.; Thompson, G.E. XPS studies of MoS₂ formation from ammonium tetrathiomolybdate solutions. *Surf. Coat. Technol.* **1997**, *91*, 200–207. [[CrossRef](#)]
57. Meng, C.H.; Liu, Z.Y.; Zhang, T.R.; Zhai, J. Layered MoS₂ nanoparticles on TiO₂ nanotubes by photocatalytic strategy as high-performance electrocatalysts for hydrogen evolution reaction. *Green Chem.* **2015**, *17*, 2764–2768. [[CrossRef](#)]
58. Koroteev, V.O.; Bulusheva, L.G.; Asanov, I.P.; Shlyakhova, E.V.; Vyalikh, D.V.; Okotrub, A.V. Charge transfer in the MoS₂/carbon nanotube composite. *J. Phys. Chem. C* **2011**, *115*, 21199–21204. [[CrossRef](#)]
59. Huang, Z.P.; Chen, Z.B.; Chen, Z.Z.; Lv, C.C.; Meng, H.; Zhang, C. Ni₁₂P₅ nanoparticles as an efficient catalyst for hydrogen generation via electrolysis and photoelectrolysis. *ACS Nano* **2014**, *8*, 8121–8129. [[CrossRef](#)] [[PubMed](#)]

60. Pan, Y.; Hu, W.H.; Liu, D.P.; Liu, Y.Q.; Liu, C.G. Carbon nanotubes decorated with nickel phosphide nanoparticles as efficient nanohybrid electrocatalysts for the hydrogen evolution reaction. *J. Mater. Chem. A* **2015**, *3*, 13087–13094. [[CrossRef](#)]
61. Kim, S.M.; Jin, S.H.; Lee, Y.J.; Lee, M.H. Design of nickel electrodes by Electrodeposition: Effect of internal stress on hydrogen evolution reaction in alkaline solutions. *Electrochim. Acta* **2017**, *252*, 67–75. [[CrossRef](#)]
62. Zeng, M.; Li, Y.G. Recent advances in heterogeneous electrocatalysts for the hydrogen evolution reaction. *J. Mater. Chem. A* **2015**, *3*, 14942–14962. [[CrossRef](#)]
63. Rosalbino, F.; Delsante, S.; Borzone, G.; Angelini, E. Electrocatalytic behaviour of Co–Ni–R (R = Rare earth metal) crystalline alloys as electrode materials for hydrogen evolution reaction in alkaline medium. *Int. J. Hydrog. Energy* **2008**, *33*, 6696–6703. [[CrossRef](#)]
64. Zheng, H.T.; Mathe, M. Hydrogen evolution reaction on single crystal WO₃/C nanoparticles supported on carbon in acid and alkaline solution. *Int. J. Hydrog. Energy* **2011**, *36*, 1960–1964. [[CrossRef](#)]
65. Kong, D.S.; Cha, J.J.; Wang, H.T.; Lee, H.R.; Cui, Y. First-row transition metal dichalcogenide catalysts for hydrogen evolution reaction. *Energy Environ. Sci.* **2013**, *6*, 3553–3558. [[CrossRef](#)]
66. Brug, G.J.; Van Den Eeden, A.L.G.; Sluyters-Rehbach, M.; Sluyters, J.H. The analysis of electrode impedances complicated by the presence of a constant phase element. *J. Electroanal. Chem. Interfacial Electrochem.* **1984**, *176*, 275–295. [[CrossRef](#)]
67. Kunhiraman, A.K.; Ramasamy, M.; Ramanathan, S. Efficient hydrogen evolution catalysis triggered by electrochemically anchored platinum nano-islands on functionalized-MWCNT. *Int. J. Hydrog. Energy* **2017**, *42*, 9881–9891. [[CrossRef](#)]
68. Wei, Z.D.; Yan, A.Z.; Feng, Y.C.; Li, L.; Sun, C.X.; Shao, Z.G.; Shen, P.K. Study of hydrogen evolution reaction on Ni–P amorphous alloy in the light of experimental and quantum chemistry. *Electrochem. Commun.* **2007**, *9*, 2709–2715. [[CrossRef](#)]
69. Hinnemann, B.; Moses, P.G.; Bonde, J.; Jørgensen, K.P.; Nielsen, J.H.; Horch, S.; Chorkendorff, I.; Nørskov, J.K. Biomimetic hydrogen evolution: MoS₂ nanoparticles as catalyst for hydrogen evolution. *J. Am. Chem. Soc.* **2005**, *127*, 5308–5309. [[CrossRef](#)] [[PubMed](#)]



© 2018 by the authors. Licensee MDPI, Basel, Switzerland. This article is an open access article distributed under the terms and conditions of the Creative Commons Attribution (CC BY) license (<http://creativecommons.org/licenses/by/4.0/>).